J. Mech. Phys. Solids 165 (2022) 104912

Contents lists available at ScienceDirect

Journal of the Mechanics and Physics of Solids

journal homepage: www.elsevier.com/locate/jmps

Measuring Terzaghi's effective stress by decoding force transmission in fluid-saturated granular media

J.E. Andrade *, Z. Gu, S. Monfared, K.A. Mac Donald, G. Ravichandran

Division of Engineering and Applied Science, California Institute of Technology, Pasadena, CA 91125, United States of America

ARTICLE INFO

Keywords:
Terzaghi effective stress
Saturated granular media
Contact forces

ABSTRACT

Force transmission between solid and fluid phases in fluid-saturated granular systems is yet to be fully resolved. This is rooted in our inability to measure inter-particle forces in opaque systems in the presence of fluids. At the same time, the concept of effective stress was introduced by Karl Terzaghi a century ago, but this empirical approach is yet to be linked to grain-scale phenomena experimentally. To this end, we derive an expression for the effective stress based on inter-particle forces and use a hybrid optical–mechanical method to directly measure the evolution of inter-particle forces and effective stress, offering a new perspective on how forces are distributed between solid and fluid phases. While our derivation and measurement of effective stress focuses on the limiting case of the Terzaghi stress, the methodology presented herein could be extended to more general situations, such as unsaturated conditions, where the micro-mechanical origin of effective stress remains elusive.

1. Introduction

Capturing the mechanical coupling between solids and fluids, trapped in the interstitial spaces, is pivotal for unraveling the complex behavior of a large number of natural and anthropogenic systems ranging from earthquakes to batteries to cells (Faunt et al., 2016; Smith and Montgomery, 2015; Odell et al., 1980; Christensen, 2010; Jiang and Lapusta, 2016; Rice et al., 2014; Cappa et al., 2019). Subsidence, a well-known phenomenon produced by depletion of underground fluids (e.g., water, oil, natural gas) (Faunt et al., 2016), occurs as mass and pressure of the interstitial fluids decrease in geologic formations giving rise to inter-granular stresses driving the deformation process. Hydraulic fracturing is driven by rapid pressure increase of interstitial fluids, exploiting natural or engineered flaws that propagate into fractures within the solid rock formation (Smith and Montgomery, 2015). In epithelial morphogenesis, cell rearrangement accompanying gastrulation is modulated by the oozing out of fluid filling the (solid) blastocoel as a result of pressure exerted by the invagination process (Odell et al., 1980). Lithium-ion batteries undergo significant expansion of its electrode materials (e.g., graphite, silicon) during charging/discharging cycles due to intercalation of lithium ions inducing fractures in the electrode and adversely impacting electrolyte transport (Christensen, 2010). In earthquake nucleation models, the coupling between stresses in the solid and pore fluid pressure is central for explaining observed phenomena such as depth of large earthquakes, flash heating, and fluid-induced seismicity, among others (Jiang and Lapusta, 2016; Rice et al., 2014; Cappa et al., 2019). For instance, Fig. 1 shows the classic example of consolidation of the Mexico City's Metropolitan Cathedral, which has settled in excess of 2.4 m as the total stress σ from the weight of the cathedral structure is transferred from the interstitial fluid to the solid skeleton (Ovando-Shelley et al., 1997). To this end, the effective behavior of such poromechanical systems across spatiotemporal scales depends intimately on the force transmission and evolution of stress partitioning between solid and fluid phases.

* Corresponding author.
E-mail address: jandrade@caltech.edu (J.E. Andrade).

https://doi.org/10.1016/j.jmps.2022.104912
Received 18 August 2021; Received in revised form 18 April 2022; Accepted 24 April 2022
Available online 14 May 2022

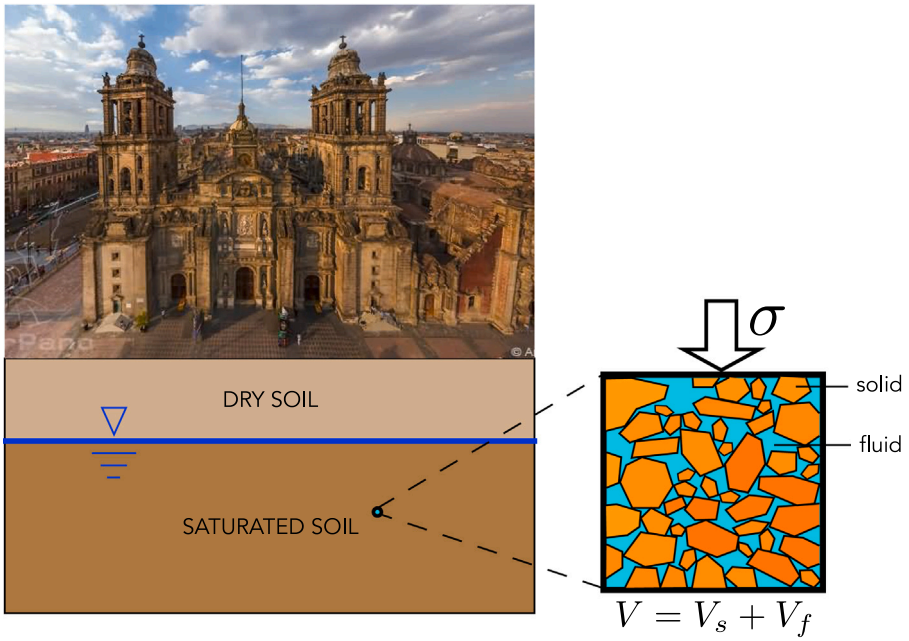

Fig. 1. The Metropolitan Cathedral in Mexico City furnishes a classic example of consolidation phenomena where the effective stress plays a central role. Since the erection of the cathedral in 1573, the total stress $\boldsymbol{\sigma}$ from the cathedral's structure has been shifting from the pore fluid pressure p to the effective stress $\boldsymbol{\sigma}'$ carried by the solid skeleton. Inset shows schematic of fully saturated granular mixture occupying a total volume V and withstanding a total stress $\boldsymbol{\sigma}$ which at any given time is split between the solid and the fluid phases occupying volumes V_s and V_f, respectively.

For a partially or fully saturated porous system in mechanical equilibrium, such as those mentioned above, the external load is carried by a combination of induced forces in both the solid domain (volume V_s) and fluid domain (volume V_f). However, the contribution of each phase, as a function of time, in this joint effort of maintaining mechanical equilibrium depends on a variety of factors (e.g., elasticity of the solids, viscosity of fluids, intrinsic permeability, etc.). One of the earliest attempts to explore this was in the 1920s by Karl Terzaghi, who dealt with this question in the context of clay deposits (Terzaghi, 1925), much like those under the cathedral in Fig. 1. He introduced the concept of effective stress $\boldsymbol{\sigma}'$, and defined it as the portion of the total stress $\boldsymbol{\sigma}$ that was carried by the solid phase or skeleton i.e.,

$$\boldsymbol{\sigma} = \boldsymbol{\sigma}' + p\mathbf{1} \tag{1}$$

with p being the pore fluid pressure and $\mathbf{1}$ signifying the identity tensor. Terzaghi's definition of effective stress is as powerful as it is simple, intuitively connected to the balance of forces and empirical models. This gave birth to the field of soil mechanics and formed the basis for what is now known as poromechanics (Coussy, 2004). Over the years, significant progress has been made in capturing the physics of fluid–solid interactions induced by a variety of complex physico-chemical phenomena at the pore scale (Coussy, 2004) by appealing to the continuum framework provided by Biot (1941) and the close-to-equilibrium thermodynamic framework of irreversible deformation proposed by Coussy (2004). Other efforts rooted in thermodynamics have shed light on the effective stress by showing it to be stress-conjugate to the total strain (Borja, 2004). However, the concept of effective stress, at the core of all these advances and outlined applications, remains empirical and rooted in phenomenological models (e.g., the Kelvin–Voigt model Simo and Hughes, 2006). Simultaneously, significant progress has been made in granular physics, particularly in measuring inter-particle forces in dry materials (Majmudar and Behringer, 2005; Daniels et al., 2017) and fully-saturated photoelastic granular systems (Ladd and Reber, 2020; Mahabadi and Jang, 2017). Nonetheless, the grain-scale origin of Terzaghi's effective stress and the measurement of inter-granular forces in opaque media and in the presence of fluids have remained elusive, hindering direct validation of the effective stress concept. Current methods indirectly *infer* the effective stress $\boldsymbol{\sigma}'$ by direct measurements of the total stress $\boldsymbol{\sigma}$ and pore fluid pressure p, and utilizing Eq. (1).

Our work hinges on the derivation of the grain-scale nature of the Terzaghi effective stress and its direct measurement. As such, this work focuses on the limiting case of applicability of the Terzaghi stress to fluid-saturated solid particle mixtures, namely:

- Fully saturated, quasi-static conditions
- Incompressible solid (particles) and fluid constituents
- Solid particles with nonconforming (point) contact

Notwithstanding these caveats, in this work we aim to answer three related, but separate fundamental questions: (1) What is the grain-scale meaning of the effective stress $\boldsymbol{\sigma}'$ as defined by Terzaghi; can it be measured directly? (2) How is a macroscopic

variable, e.g., $\boldsymbol{\sigma}'$, related to grain-scale forces? (3) How do grain-scale forces and stresses evolve with time in fluid-saturated systems? Answering these questions is central to understanding force transmission in fluid saturated granular systems, its relationship with effective stresses and ultimately mechanical behavior in a range of applications such as those mentioned above.

2. Methods

This section summarizes three key ingredients used to directly measure the Terzaghi effective stress $\boldsymbol{\sigma}'$: (i) theoretical derivation of the effective stress as a function of the intergranular forces, (ii) a simple 1D consolidation model for validating the experimental setup, and (iii) the experimental setup and measurements for computing the effective stress under classic 1D consolidation.

2.1. Derivation of effective stress as a function of intergranular forces

Our point of departure from the conventional approach is the well-established volume average of the stress (i.e., $\bar{\boldsymbol{\sigma}} := 1/V \int_V \boldsymbol{\sigma}(\boldsymbol{x})\, \mathrm{d}V$) in a fully-saturated granular system of total volume V as shown in the inset in Fig. 1. The classic additive decomposition of partial stresses states (Andrade and Borja, 2007):

$$\bar{\boldsymbol{\sigma}} = \bar{\boldsymbol{\sigma}}^s + \bar{\boldsymbol{\sigma}}^f \tag{2}$$

where each partial stress is simply the volume average of the (true) stress field in the corresponding phase occupying a volume V_s for the solid and V_f for the fluid. The additive decomposition of partial stresses is a classic result in poromechanics and does not require any phenomenological or intuitive assumptions (Andrade and Borja, 2007; Borja, 2004; Atkin and Craine, 1976; Prevost, 1980). Further, assuming constant pore fluid pressure, one can show that $\bar{\boldsymbol{\sigma}}^f = \phi^f p\mathbf{1}$, hence:

$$\bar{\boldsymbol{\sigma}} = \bar{\boldsymbol{\sigma}}^s + \phi^f p\mathbf{1} \tag{3}$$

where $\phi^f := V_f/V$ is the volume fraction occupied by the fluid phase, which in the fully-saturated condition coincides with the porosity. By comparing Eq. (2) and the definition of effective stress given by Terzaghi in Eq. (1), one can obtain a relation between the effective stress and the partial solid stress, i.e., $\boldsymbol{\sigma}' = \bar{\boldsymbol{\sigma}}^s - \phi^s p\mathbf{1}$, where $\phi^s := V_s/V$ is the volume fraction of the solid and $\phi^s + \phi^f = 1$. It is important to note that this latter result is not a grain-scale definition of the effective stress and simply follows by comparison.

In order to find a grain-scale definition of Terzaghi's effective stress $\boldsymbol{\sigma}'$, let us consider a granular medium, such as the one described at the end of the Introduction, with N solid particles, fully saturated and in equilibrium with an incompressible interstitial fluid, as shown in Fig. 2A, B. For particle i, conservation of Euler's linear and angular momenta yields:

$$\sum_{\alpha=1}^{N_i^c} \boldsymbol{f}^\alpha = \mathbf{0} \tag{4}$$

$$\sum_{\alpha=1}^{N_i^c} \boldsymbol{f}^\alpha \times \boldsymbol{x}^\alpha = \mathbf{0} \tag{5}$$

where $\boldsymbol{f}^\alpha$ is a contact (external) force at contact point $\boldsymbol{x}^\alpha$ with N_i^c contact points acting on particle i (see Fig. 2C). Here we assume that the fluid is in equilibrium at a constant pore pressure p with its surface integral vanishing and not contributing to angular momentum. Similarly, (pointwise) balance of linear momentum in particle i reads:

$$\boldsymbol{\nabla} \cdot \boldsymbol{\sigma}_i(\boldsymbol{x}) = \mathbf{0} \qquad \forall \boldsymbol{x} \in \Omega_i \tag{6}$$

Where $\boldsymbol{\sigma}_i(\boldsymbol{x})$ denotes the stress field in particle i with its domain delineated by Ω_i. For a fully saturated system, composed of solid (Ω_s) and fluid (Ω_f) domains, the total average stress can be written as follows:

$$\bar{\boldsymbol{\sigma}} := \frac{1}{V}\int_V \boldsymbol{\sigma}(\boldsymbol{x})\, \mathrm{d}V; \;\; \boldsymbol{\sigma}(\boldsymbol{x}) = \begin{cases} \boldsymbol{\sigma}_f(\boldsymbol{x}) & \forall \boldsymbol{x} \in \Omega_f \\ \boldsymbol{\sigma}_s(\boldsymbol{x}) & \forall \boldsymbol{x} \in \Omega_s \;\; (\Omega_i \subset \Omega_s) \end{cases} \tag{7}$$

We denote the (true) average stress within the solid and fluid domains as $\bar{\boldsymbol{\sigma}}_s$ and $\bar{\boldsymbol{\sigma}}_f$, respectively, and Eq. (7) can be written as (cf. Eq. (2)):

$$\bar{\boldsymbol{\sigma}} = \frac{1}{V}(V_s\bar{\boldsymbol{\sigma}}_s + V_f\bar{\boldsymbol{\sigma}}_f) = \phi^s\bar{\boldsymbol{\sigma}}_s + \phi^f\bar{\boldsymbol{\sigma}}_f = \bar{\boldsymbol{\sigma}}^s + \bar{\boldsymbol{\sigma}}^f \tag{8}$$

where V_s and V_f are the volumes of the solid and fluid phases, ϕ^s and ϕ^f are the corresponding volume fractions occupied by the two phases. The multiplication of the volume fraction and the corresponding (true) average stress is known as the partial stress, denoted as $\bar{\boldsymbol{\sigma}}^s$ and $\bar{\boldsymbol{\sigma}}^f$, respectively. In a fluid, it can be shown that $\boldsymbol{\sigma}_f(\boldsymbol{x}) = p(\boldsymbol{x})\mathbf{1}$. Also, if pore pressure $p(\boldsymbol{x}) = p$ (constant), the average stress of the fluid phase is:

$$\bar{\boldsymbol{\sigma}}_f = \frac{1}{V_f}\int_{V_f} p(\boldsymbol{x})\mathbf{1}\, \mathrm{d}V_f = p\mathbf{1} \tag{9}$$

Furthermore, the average stress of the solid phase can be expressed as:

$$\bar{\boldsymbol{\sigma}}_s = \frac{1}{V_s}\sum_{i=1}^{N}\int_{V_i} \boldsymbol{\sigma}_i(\boldsymbol{x})\, \mathrm{d}V_i = \frac{1}{V_s}\sum_{i=1}^{N} V_i\bar{\boldsymbol{\sigma}}_i \tag{10}$$

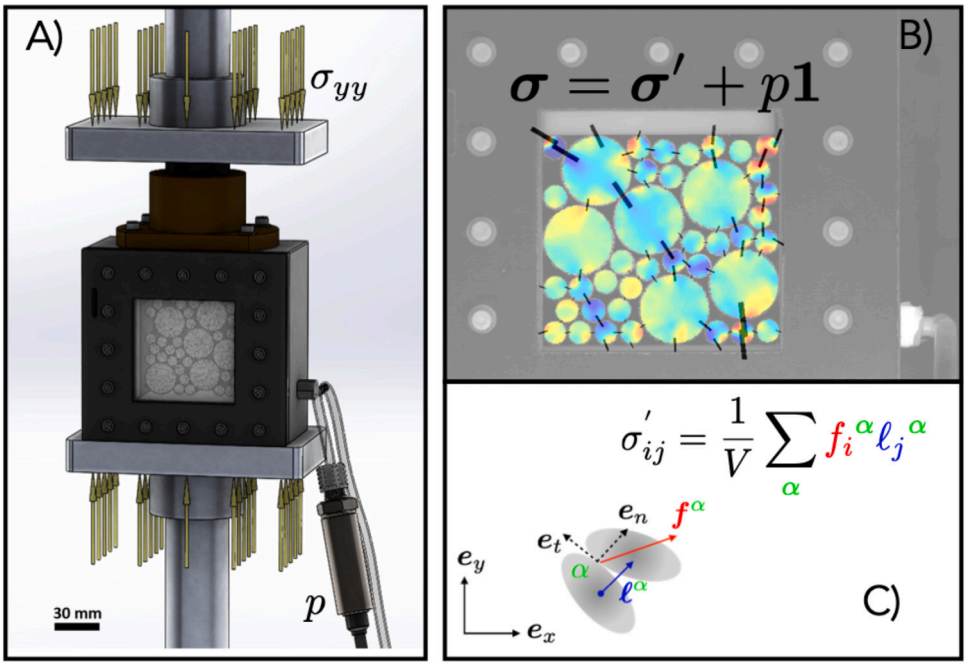

Fig. 2. Hybrid optical–mechanical approach to establish the relation between effective stress and inter-particle forces. (A) The experimental cell (quasi-2D) where a total vertical stress σ_{yy} is imposed. The drainage process is controlled via a valve and the fluid pore pressure p is measured with a pressure sensor located at the bottom right corner of the cell. (B) An example of the developed force chains (black lines, whose thickness relates to magnitude and direction is coaxial to inter-particle forces) for a given configuration utilizing the Granular Element Method (GEM) based on strains obtained from Digital Image Correlation (DIC) analysis. This allows measurement of the inter-particle forces in the solid phase and, consequently, effective stress tensor via Eq. (15), previously inaccessible in saturated granular systems. (C) Theoretical backbone of the framework linking inter-particle forces $\boldsymbol{f}^{\alpha}$, at the α-contact point, and branch vector $\boldsymbol{\ell}^{\alpha}$ to the effective stress in the solid (Christoffersen et al., 1981), averaging over a volume V.

where V_i denotes volume associated with domain Ω_i, $\sum_{i=1}^{N} V_i = V_s$ and $\bar{\boldsymbol{\sigma}}_i$ represents the volume-average stress of particle i. For a discrete system in equilibrium, employing Eq. (6) and the divergence theorem in the expression of $\bar{\boldsymbol{\sigma}}_i$ yields (Christoffersen et al., 1981):

$$\bar{\boldsymbol{\sigma}}_i = \frac{1}{V_i}\int_{S_i} \mathrm{sym}\,(\boldsymbol{t}\otimes\boldsymbol{x})\,\mathrm{d}S_i = \frac{1}{V_i}\left\{\sum_{\alpha=1}^{N_i^c} \mathrm{sym}\,(\boldsymbol{f}^{\alpha}\otimes\boldsymbol{x}^{\alpha}) + \int_{S_i} \hat{\boldsymbol{n}}\cdot(p(\boldsymbol{x})\mathbf{1}\otimes\boldsymbol{x})\,dS_i\right\} \tag{11}$$

where $\boldsymbol{t}$ is the traction at point $\boldsymbol{x}$, with $\boldsymbol{x}\in S_i$, and $p(\boldsymbol{x})$ is the pore fluid pressure acting on the surface S_i, whose point-wise normal vector is $\hat{\boldsymbol{n}}(\boldsymbol{x})$. The symbol 'sym' signifies the symmetric operator. We have also utilized the standard assumption that forces $\boldsymbol{f}^{\alpha}$ are applied pointwise at location $\boldsymbol{x}^{\alpha}$, see Fig. 2C. Again, given a constant pore pressure $p(\boldsymbol{x})$, employing the divergence theorem into the fluid pressure term, the average stress $\bar{\boldsymbol{\sigma}}_i$ can be further written as:

$$\bar{\boldsymbol{\sigma}}_i = \frac{1}{V_i}\sum_{\alpha=1}^{N_i^c} \mathrm{sym}(\boldsymbol{f}^{\alpha}\otimes\boldsymbol{x}^{\alpha}) + p\mathbf{1} \tag{12}$$

Substituting equation Eq. (12) into (10), and then Eq. (9) and (10) into Eq. (8) leads to a new expression of the total average stress $\bar{\boldsymbol{\sigma}}$:

$$\bar{\boldsymbol{\sigma}} = \frac{1}{V}\sum_{\alpha=1}^{N^c} \mathrm{sym}(\boldsymbol{f}^{\alpha}\otimes\boldsymbol{\ell}^{\alpha}) + (\phi^s+\phi^f)p\mathbf{1} \tag{13}$$

where N^c is the number of contacts in the entire domain and $\boldsymbol{\ell}^{\alpha}$ is the branch vector connecting the centroid of the particles in contact at contact point α, as shown in Fig. 2C. Furthermore, $\Omega = \Omega_s \cup \Omega_f$ ($\Omega_s \cap \Omega_f = \emptyset$) constitutes the entire domain of the mixture. Additionally, partition of unity holds such that $\phi^s + \phi^f = 1$. Finally, the total average stress becomes:

$$\bar{\boldsymbol{\sigma}} = \frac{1}{V}\sum_{\alpha=1}^{N^c} \mathrm{sym}(\boldsymbol{f}^{\alpha}\otimes\boldsymbol{\ell}^{\alpha}) + p\mathbf{1} \tag{14}$$

Thus, the partial solid stress for a granular medium can be expressed as $\bar{\boldsymbol{\sigma}}^s = 1/V\sum_{\alpha}\boldsymbol{f}^{\alpha}\otimes\boldsymbol{\ell}^{\alpha} + \phi^s p\mathbf{1}$, where, as shown in Fig. 2, the inter-particle forces $\boldsymbol{f}^{\alpha}$ and branch vectors $\boldsymbol{\ell}^{\alpha}$ are defined at contact point α, and summed over the entire volume V. Notice

there is a contribution to the partial solid stress stemming from the pore fluid pressure and scaled by the solid volume fraction $\phi^s := V_s/V$. Finally, Eq. (2) with the help of Eq. (14) can be written as:

$$\bar{\boldsymbol{\sigma}} = \underbrace{1/V \sum_{\alpha=1}^{N^c} \text{sym}(\boldsymbol{f}^\alpha \otimes \boldsymbol{\ell}^\alpha)}_{\bar{\boldsymbol{\sigma}}'} + p\mathbf{1} = \boldsymbol{\sigma}' + p\mathbf{1} \tag{15}$$

We recognize the term $\bar{\boldsymbol{\sigma}}'$ as the *drained* stress expression obtained by Christoffersen et al. (1981) and shown schematically in Fig. 2C. Also, comparing Eq. (15) with the Terzaghi expression in Eq. (1) we can see that they are form-identical and that the effective stress

$$\boldsymbol{\sigma}' := \frac{1}{V} \sum_{\alpha=1}^{N^c} \text{sym}(\boldsymbol{f}^\alpha \otimes \boldsymbol{\ell}^\alpha) \tag{16}$$

has a clear linkage to grain-scale properties such as forces and branch vectors; an intuitive, but heretofore unproven result. For example, previous discrete element models for fluid-saturated granular media use Eq. (16) as the expression for effective stress (Galindo-Torres et al., 2018; Kuhn and Daouadji, 2020), without derivation. We exploit this linkage to measure the forces at the grain-scale in saturated granular media and thereby measure the effective stress directly for the first time, in the context of 1D consolidation, whose analytical solution is well-known.

Remark 1. It is important to note that the expression obtained in Eq. (16) is form-identical to the expression obtained for the Cauchy stress for dry (drained) granular systems and derived in previous seminal contributions (Rothenburg and Salvadurai, 1981; Christoffersen et al., 1981). Hence the idea of granular forces contributing to macroscopic stress is not new. However, our work adds to the previous body of work by looking into fluid saturated systems. All previous work has either focused on formal derivations of Cauchy stress for dry systems or have applied the Cauchy stress as the effective stress without justification. Notwithstanding these formalisms, the main contribution of the current work is the use of Eq. (16) to measure the effective stresses directly.

Remark 2. The assumption of constant pore pressure p is compatible with the fluid being in equilibrium. However, in the classic 1D consolidation problem shown in the next section, the pressure is homogeneous for most of the domain (cf. Eq (17)), except near the drainage boundary where the pressure profile drops. In the experiments described herein, the drainage valve near the bottom is not fully open, allowing for measurable, non-zero pore pressures and a quasi-homogeneous pressure profile. Therefore, the actual conditions of the experiment are somewhat in between fully homogeneous pressures and those observed in the consolidation problem. This is one possible source of error in the results shown in Fig. 4A, especially early on in the consolidation process when pore pressure carries the lion share of the total stress.

2.2. Analytical solution of one-dimensional consolidation

The analytical solution corresponding to Terzaghi's one-dimensional consolidation problem (Terzaghi, 1925) is well known and can be obtained by considering a porous system composed of isotropic, linear poroelastic solid and for the asymptotic case that corresponds to incompressible solids and fluids. To this end, one can solve for pressure and displacement fields. We utilize the analytical solution to validate our experimental data. The physical parameters controlling the 1D consolidation problem are the consolidation coefficient c_v and constrained modulus E. Furthermore, the results can be written in dimensionless form ($\bar{t} = c_v t/(4L^2)$, $\bar{y} = y/L$):

$$p(\bar{y}, \bar{t}) = \sigma_{yy} \sum_{n\in\{2k+1|k\in\mathbb{N}\}} \frac{4}{n\pi} \sin\left(\frac{n\pi}{2}\bar{y}\right) \exp\left(-(n\pi)^2\bar{t}\right) \tag{17}$$

$$u(\bar{y}, \bar{t}) = -\frac{\sigma_{yy}}{E} \sum_{n\in\{2k+1|k\in\mathbb{N}\}} \frac{8L}{(n\pi)^2} \left[\cos(\frac{n\pi}{2}\bar{y}) - 1\right] \left[\exp(-(n\pi)^2\bar{t}) - 1\right] \tag{18}$$

Finally, the settlement can be obtained from the displacements as follows:

$$s(\bar{t}) = \frac{1}{L} u(\bar{y} = 1, \bar{t}) = \frac{\sigma_{yy}}{E} \sum_{n\in\{2k+1|k\in\mathbb{N}\}} \frac{8}{(n\pi)^2} \left[\exp(-(n\pi)^2\bar{t}) - 1\right] \tag{19}$$

where $\sum_{n\in\{2k+1|k\in\mathbb{N}\}} \frac{8}{n^2\pi^2} = 1$.

In this work, we obtained the constrained modulus E by discrete element modeling of the drained system (see Appendix B), and independently by taking the ratio of the total stress to the total strain observed in the experiments (cf., Fig. 4C), with E ranging from about 3.3–4.0 MPa; we fitted the consolidation coefficient since we did not have the true permeability of the system. As shown in Fig. 4, we used $E = 3.49$ MPa and $c_v = 304 \times 10^{-6}$ m^2/s to fit experimental values.

Remark 3. The dimensionless pressure in Eq. (17) and the settlement expression in Eq. (19) furnish analytical validation for the experimental results provided in the next section. As can be seen, the constrained modulus E affects the amount of maximum settlement and the coefficient of consolidation c_v scales the dimensionless time axis. Hence, at any point along the domain $y \in (0, L]$, the pressure evolution in time can be plotted using Eq. (17).

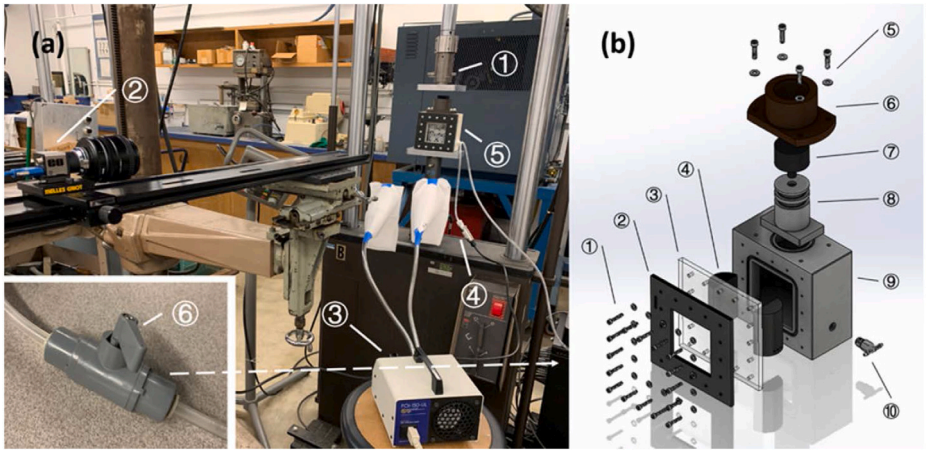

Fig. 3. (a) Experimental setup: 1. Loading frame, 2. Camera, 3. Fiber optic illuminator, 4. Pressure sensor, 5. Container, 6. Valve (not shown in the large picture, shown in the inset). (b) Exploded view of the container: 1. #6-32 screws and washers, 2. Window bracket, 3. Transparent window, 4. Sidewalls, 5. #10-32 screws and washers, 6. Piston chamber, 7. Piston cap, 8. Piston, 9. Box, 10. Branch tube fitting.

2.3. Experimental setup for fully saturated consolidation experiments

In this section, we describe the experimental device we developed to (i) physically model the 1D consolidation problem solved in the previous section, (ii) validate the experimental setup by comparing our measurements with those obtained analytically, and (iii) measure interparticle forces that enable us to directly measure effective stress using Eq. (16). The experimental set up shown in Fig. 3A consists of a servo-hydraulic loading frame (MTS material test system, Model 358.10), load transducer (Model 11019), a CCD camera (Nikon AF Nikkor 50 mm), a fiber optic illuminator (Cole-Parmer, Model 41500-50) with a diffuser, a pressure sensor (OMEGA PX309-015GV), a valve (Push-to-Connect PVC On/Off valve, 1/4" OD tube) and a container that can hold a fully saturated and pressurized granular packing.

The container, as shown in Fig. 3B, includes a box, a transparent window, a window bracket, two sidewalls, a piston, a piston cap, a piston chamber, and a branch tube fitting. Since the shape of the box is complex and difficult to machine, the box, the window bracket as well as the sidewalls were 3D printed using a Stratasys Connex3 Objet350 printer. The box was made of VeroWhitePlus, while the window bracket and sidewalls were made of VeroBlackPlus. Additionally, the piston, the piston cap and the piston chamber were machined out of delrin and delrin acetal AF resin rods. A polycarbonate plate was used as the transparent window to enable optical imaging. Chemical-resistant Viton fluoroelastomer O-Rings were utilized to seal the whole setup and nylon socket head screws were used to hold all the parts together. To facilitate free drainage, a chemical-resistant barbed tube fitting was placed on the side of the box.

To study various configurations at the grain-scale, two types of multipurpose neoprene rubber rods were employed. These rod-shaped particles are assumed to be linear elastic and incompressible, i.e., Poisson's ratio ≈ 0.5. The material used for the large particles (diameter = 20 mm, length = 25.4 mm) has a Young's modulus of 55 MPa, and the material used for the small particles (diameter = 7 mm, length = 25.4 mm) has a Young's modulus of 21.5 MPa, which we independently measured. Additionally, for these materials, the reported Coulomb friction coefficient is $\mu = 0.6$ (Hurley et al., 2014). The granular packings used in the experiments contain 6 large particles and 34 or 35 small particles. To achieve an appropriate grayscale speckle pattern for Digital Image Correlation (DIC) analysis, white multi-surface paint was used to generate speckle patterns on the black rubber particles.

3. Results

As illustrated in Fig. 2, we use a hybrid optical–mechanical approach to measure inter-particle forces and, via Eq. (16), the effective stress. To validate our approach, we reproduce the classic consolidation problem (Fig. 2A). This entails application of a constant stress σ_{yy} in the vertical direction, which is partitioned between the fluid pressure p and the effective stress σ'_{yy} carried by the solid (Terzaghi, 1925). In the classic consolidation problem, the time evolution of the pore fluid pressure $\dot{p}$ is modeled as a parabolic partial differential equation (cf., Section 2.2). The effective stress is typically inferred as $\sigma'_{yy} = \sigma_{yy} - p$, never directly measured experimentally—varying from zero at the beginning to the total stress at the end of the consolidation process. This indirect estimation of the effective stress is a consequence of the lack of a grain-scale definition of effective stress and the inability to measure inter-particle forces in the presence of fluids. Here, we independently measure the fluid pressure and the effective stress evolutions in time and demonstrate that they account for the total applied stress, as postulated by Terzaghi and formalized in Eq. (16). With this unprecedented access to local information at the grain scale, we are able to explain how inter-particle forces are distributed in the presence of fluids and what controls the evolution of effective stress, questions that cannot be addressed using the current approaches.

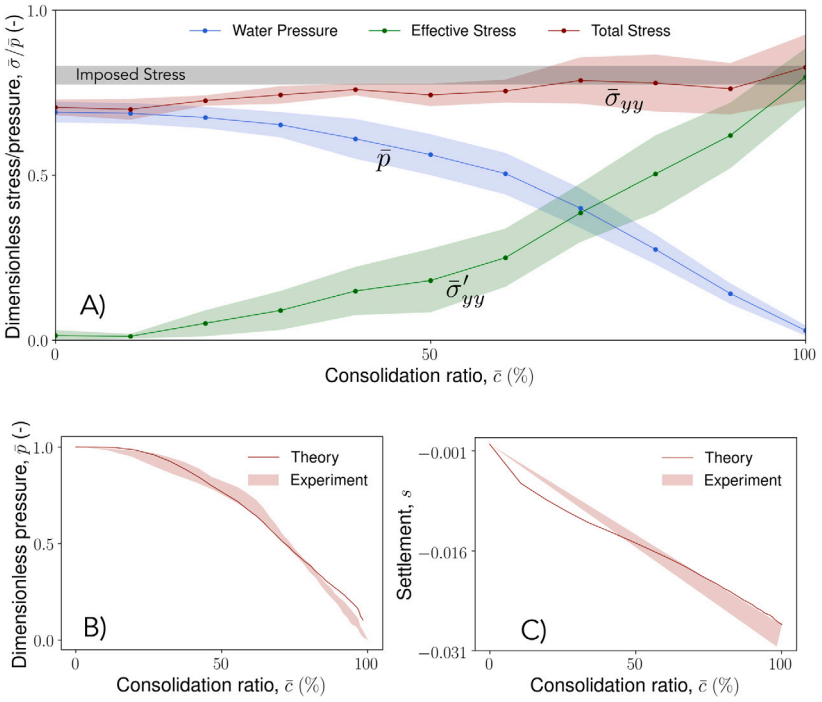

Fig. 4. Experimental results with the shaded region capturing the range of results for various granular configurations. (A) Evolution of total vertical stress $\bar{\sigma}_{yy}$, fluid pressure $\bar{p}$, and effective vertical stress $\bar{\sigma}'_{yy}$ as a function of consolidation ratio $\bar{c}$. In contrast to previous studies, the evolution of effective stresses is measured directly from the inter-particle forces (see Eq. (16) and Fig. 2). Shaded region of imposed stress represents standard deviation from desired stress level. (B), (C) Comparison between the measured pore pressure $\bar{p}$ and the settlement s, respectively, with their counterparts of the analytical solution (Eqs. (17) and (19)) as a function of the consolidation ratio $\bar{c}$ ($E = 3.49$ MPa and $c_v = 304 \times 10^{-6}$ m^2/s). Results serve as validation of the effective stress measurements and the experimental setup: in (A) the total stress is approximately constant and additively decomposed between effective stress (measured) and pore pressure (measured); in (B) the evolution of pore pressure $\bar{p}$ measured at the bottom of the specimen corresponds to the pore pressure evaluated using Eq. (17); in (C) the evolution of settlement measured in the specimens matches the settlement evaluated using Eq. (19).

To measure the inter-particle forces, we rely on the granular element method (GEM) (Hurley et al., 2014) developed by the authors in the context of dry granular matter. We measure the strain in each rod-shaped particle using digital image correlation (DIC) (Sutton et al., 2009). The transparent wall in the apparatus (Fig. 2) allows us to employ simple optical methods to measure planar deformation, which is input into GEM to deduce the inter-particle forces. Other techniques of measuring average strains (e.g., X-ray diffraction, confocal microscopy) in the particles could also be employed (Donald and Ravichandran, 2019; Hurley et al., 2016). Thus, the effective stress and its evolution as a function of time is measured directly from inter-particle forces obtained from GEM. The volume V of the cell is important and it needs to be large enough such that the effective stress matches the imposed external stress (Zohdi and Wriggers, 2005) (see Discussion section). Additionally, the apparatus (Fig. 2) is equipped with a pressure gauge, located at the drainage orifice (Fig. 3A), to measure the fluid pressure as a function of time while the total stress is held constant by externally applied servo-controlled load. The measured fluid pressure is assumed representative of the entire cell, which is a good assumption under quasi-static conditions. In addition, the pore pressure is analytically evaluated using Eq. (17). A drainage valve on the side of the apparatus allows for slow fluid transport and pressure diffusion leading to the consolidation process. This in turn provides direct access to the physics of force sharing between the fluid and solid phases, which controls the problem.

Fig. 4A depicts the results obtained from the quasi-2D consolidation experiments that were conducted using the apparatus in Fig. 2A. The top figure shows the evolution of stresses and the pressure for three representative experiments with different granular configurations. The solid lines in Fig. 4 represent the average results for three different experiments while the shaded region corresponds to the calculated standard deviation (see Fig. A.1 for the same plot for each individual experiment). They are plotted as a function of the consolidation ratio $\bar{c}$, defined as the ratio between the current deformation over the total deformation resulting from the consolidation process. One can observe that the total stress $\bar{\sigma}_{yy}$, the sum of the contributions of the fluid pore pressure $\bar{p}$ and the effective stress $\bar{\sigma}'_{yy}$, is approximately constant (as prescribed at the top boundary). This result serves as validation of our approach since the effective stress is measured using Eq. (16), and independent of the pore pressure $\bar{p}$ measurement. Initially, as theoretically expected, the pore fluid carries the majority of the load. As the consolidation proceeds, the pore fluid pressure decreases and the effective stress increases, a manifestation of increase in inter-particle forces. A time lapse of the experiment (see Movie S1) highlights the evolution of inter-particle forces. When the consolidation process is around 75% complete, the effective stress and pore pressures appear to share load equally. At the end of the consolidation, the fluid pressure is entirely dissipated, and the effective stress of the solid carries the total external load. At this point, the system is completely drained, and pore pressure does not affect the mechanical response.

Remark 4. It is important to note that the early portion of the total stress $\bar{\sigma}_{yy}$ measured in the experiments and reported in Fig. 4A shows a gap or difference with respect to the imposed stress. This difference is mostly present in the early portion of the consolidation process (close to $\bar{c} = 0\%$) when the pore pressure $\bar{p}$ dominates the total stress. This error is likely due to the pressure gauge being located near the entrance of the drainage valve, which would naturally induce lower pressures necessary for (slow) fluid flow. The error decreases passed $\bar{c} = 50\%$ as the pore pressure $\bar{p}$ drops and the effective stress $\bar{\sigma}'_{yy}$ starts to dominate the response.

The consolidation problem serves as a validation exercise for our newly derived expression for effective stress (Eq. (16)). This is achieved by comparing the evolution of both the pore pressure $\bar{p}$ and the settlement s against the well-known analytical solutions for consolidation (Eqs. (17) and (19)). Fig. 4B shows comparisons between the fluid pressure measured in the experiments and the analytical solution furnished by Eq. (17). As noted earlier, the analytical solution for pore pressure depends on the coefficient of consolidation, which here is calibrated to capture the flow rate of the experiments. Similarly, in Fig. 4C, the settlement s for the granular assembly in the experiment is compared to the analytical solution furnished by Eq. (19). Also, the maximum settlement (at $\bar{c} = 100\%$) is controlled by the constrained modulus E. As shown in Fig. 4, the consolidation coefficient c_v and the constrained elastic modulus E yield values that are well within those reported in the literature (Holtz et al., 1981). Thus, our approach to measure inter-particle forces is validated with well-known analytical solutions of the consolidation problem. This enables us to make a direct link between the evolution of inter-particle forces and effective stresses at the core of many poromechanical systems. It is important to note that while our results explicitly link the effective stress model developed by Terzaghi to grain-scale phenomena, our approach does not rely on phenomenological assumptions, and holds for general cases beyond the consolidation example presented here (e.g., 3D loading).

4. Discussion

We now turn our attention to the following question: how are forces distributed in the particles – over time – in the presence of fluids? We use our physics-based model to decode the mechanism controlling evolution of forces in the presence of fluids, in particular the case of a fully saturated granular medium. Taking the time evolution of the theoretical expression for the total stress in Eq. (15), the time evolution of the effective stress is seen as a combination of the time evolutions of the inter-particle forces and the branch vectors enabling such contacts i.e., $\dot{\boldsymbol{\sigma}}' = 1/V \sum_\alpha (\dot{\boldsymbol{f}}^\alpha \otimes \boldsymbol{\ell}^\alpha + \boldsymbol{f}^\alpha \otimes \dot{\boldsymbol{\ell}}^\alpha)$. In a geometrically frustrated system, i.e., one where grains are not allowed to reconfigure, like the one shown in Fig. 2, the branch vectors do not evolve significantly since the particles are geometrically constrained and unable to rearrange. Therefore, in such a system, the evolution of the effective stress is dominated by the evolution of inter-particle forces such that

$$\dot{\boldsymbol{\sigma}}' \approx \frac{1}{V} \sum_\alpha \dot{\boldsymbol{f}}^\alpha \otimes \boldsymbol{\ell}^\alpha \tag{20}$$

With a constant total stress, the reduction in pore pressure must be directly matched by a corresponding increase in effective stress (i.e., $\dot{p} = -\dot{\sigma}'_{yy} \approx -1/V \sum_\alpha \dot{f}^\alpha_y \ell^\alpha_y$). As shown in Fig. 5A, the pore pressure evolution is countered by the evolution of the vertical effective stress. This in turn relies on the evolution of horizontal and vertical force chains carried by contacts with largest components in those preferred directions. We conjecture that the orientation of the branch vectors acts as a catalyst in the evolution of inter-granular energy density, since contacts with existing components in the vertical direction can do more work for a given increment of force. It is important to note that neither phenomenology nor analogs with drained systems can provide insights into the question of force distribution. The former can only provide the current effective stress by inference or via constrained moduli and the latter can only explain force distribution in dry systems. The effect of interstitial fluids is to control the rate of evolution in fluid-saturated systems, thereby affecting the force distribution, including under equivalent effective stresses. Even in dry systems, the same macroscopic stress may result in a different force distribution. This is only exacerbated in diffusion-controlled fluid-saturated systems.

Fig. 5B shows a scatter plot of relative contact orientations and the force magnitudes associated with them for one of the experiments conducted in our study (see Fig. A.2 for the same plot for each of the experiments conducted in this study). Representative of the other experiments, this plot suggests that, initially, the distribution of force magnitudes is fairly uniform along available branch vectors. As the energy density rate associated with the inter-particle forces peaks (Fig. 5A), the distribution of forces displays an increase in magnitude in the direction of vertically aligned branch vectors (Fig. 5B). This supports our conjecture that branch vectors play the role of catalysts in the evolution of inter-granular energy density. By the end of the consolidation process, the forces reach peak magnitude, with strong directionality along the branch vectors that point along the direction of macroscopic load application. Remarkably, about 5% of particle contacts are responsible for 95th (p95) percentile of force distribution during the experiment (Fig. A.1). These contacts are clearly biased towards the vertical direction as the pore pressure diffusion shifts the load-carrying burden from the fluid phase onto the solid phase.

Two issues come to mind that have important implications for the results presented herein. First, volume averaging equations require a representative unit cell of large enough volume V such that one can properly define continuum variables such as the effective stress $\boldsymbol{\sigma}'$. Clearly, results would vary slightly with different sizes of V. In this study, we do not analyze in depth the effects of V, rather we use the notion that internal stress calculated using volume averaging, are equal to external applied stresses when the volume V is appropriate (Andrade et al., 2012; Zohdi and Wriggers, 2005). In this particular case, the effective stress values at the end of consolidation perfectly match the external stress applied at the boundary, and all other continuum results (e.g., pore pressure p and settlement s) match the continuum theoretical results (see Fig. 4). Second, the effect of fluid-saturation in the inter-granular force distribution and evolution should be addressed. It is tempting to extrapolate that, since the effective stress is related to the

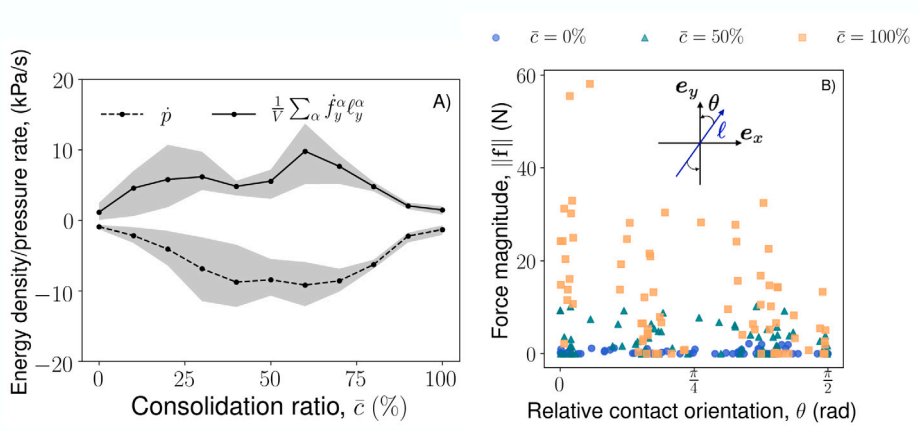

Fig. 5. Mechanism controlling the evolution of forces and effective stress with time (consolidation) in a fully saturated granular system. (A) Evolution of pore pressure countered by the work rate done by the vertical forces in three different experiments. The solid line represents the average values of the three experiments while the shaded region indicates the calculated standard deviation. (B) Scatter plot of force magnitude and contact orientation relative to the direction of load application, showing clear increases in magnitude of force as consolidation evolves, especially in the direction of loading ($\theta = 0$).

inter-granular contact forces just like in the fully drained case, hence the force distribution should be the same regardless of the fluid for a given level of effective stress. While tempting, this is not necessarily the case, as seen in Eq. (20), since the time evolution of effective stress is controlled by the time evolution of the pore pressure such that $\dot{\sigma}'_{yy} \sim -\dot{p}$ (see Fig. 5A) and, therefore, the fluid pressure diffusion affects the time evolution of the inter-granular forces; the latter being path-dependent.

The linkage of effective stress and the force measurements in the presence of fluids allows us to reconstruct the evolution of effective stress, pore fluid pressure, and total stress – independently – for the first time since the concept of effective stress was introduced a century ago. Specifically, we focused our efforts to validate our approach against the limiting case that corresponds to Terzaghi's definition for effective stress. However, our hybrid approach is versatile and can be further developed to explore complex poromechanical systems, unraveling the intimate coupling between inter-particle forces and solid stresses in the presence of fluids. For example, inter-cellular forces could be directly measured using a similar hybrid approach, with different computational and experimental ingredients, to complement the existing models for capturing cell behavior (Notbohm et al., 2012; Sunyer et al., 2016).

Furthermore, in a departure from continuum roots, a recent discrete formulation of poroelasticity enables direct access to Biot pore pressure coupling coefficients (Monfared et al., 2017), which drive diffusion in deformable solids due to inter-particle forces. Thus, poroelastic diffusion can be considered as a design parameter for tissue engineering and drug delivery applications. This hybrid framework also offers a path to directly probe capillary pressures in wet, disordered granular systems utilizing for example a recent computational framework that can account for the formation, growth and coalescence of liquid clusters while properly mapping the spatial distribution of capillary forces (Monfared et al., 2020). Such capability can provide tools in granular physics to robustly define effective stress in partially saturated porous media (Lu, 2020). So far, most models have relied on validating only the kinematics given the dearth of experimental measurement of forces. Our results open the door for simultaneously accessing kinematics (deformation) and kinetics (forces) in poromechanical systems, which can facilitate the formulation of predictive models that capture the underlying physics of these complex systems.

CRediT authorship contribution statement

J.E. Andrade: Conceptualization, Methodology, Writing, Supervision. **Z. Gu:** Methodology, Validation, Investigation, Data curation. **S. Monfared:** Methodology, Validation, Writing. **K.A. Mac Donald:** Methodology, Validation, Investigation. **G. Ravichandran:** Conceptualization, Methodology, Supervision, Writing.

Declaration of competing interest

The authors declare that they have no known competing financial interests or personal relationships that could have appeared to influence the work reported in this paper.

Acknowledgment

This research was partially supported by the Army Research Office, United States of America Multidisciplinary University Research Initiative, United States of America Grant No. W911NF-19-1-0245. This support is gratefully acknowledged.

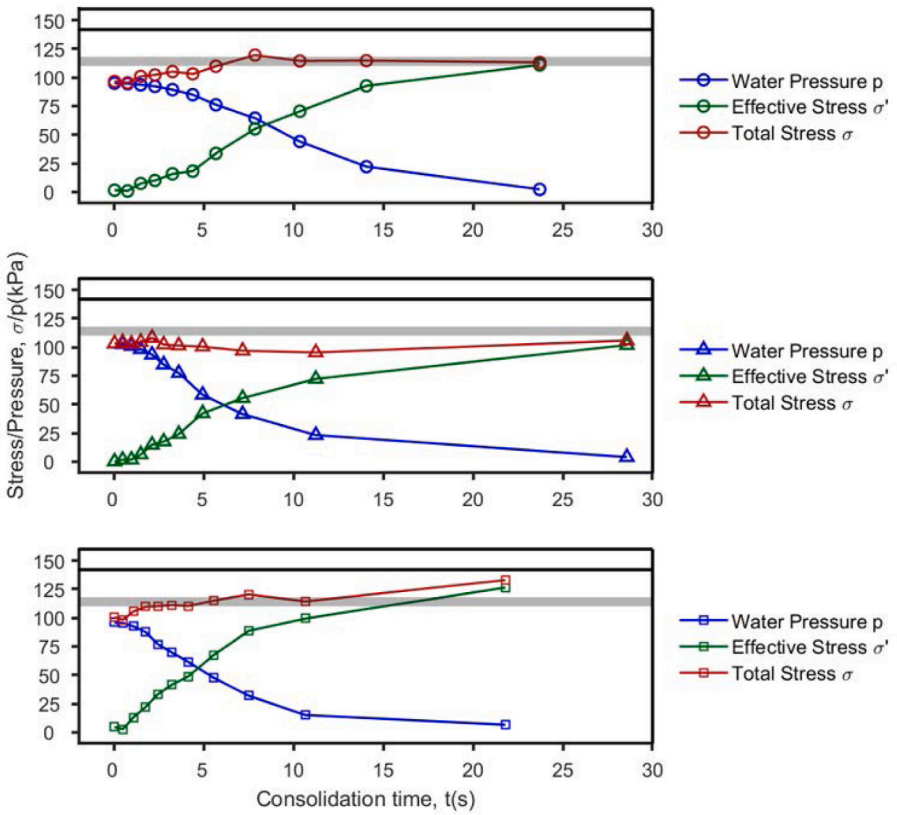

Fig. A.1. Force percentiles and the contact percentage associated with those percentiles for experiments 1–3 (top-to-bottom). The data for each plot represents all the time-series for that experiment. For example, for experiment 3, the forces great than the 20th percentile are carried by about 80% of the contacts.

Appendix A. Figures

See Figs. A.1–A.3.

Appendix B. Discrete element method simulation

We compared the fitted constrained Young's modulus for the drained solid skeleton with results from simulations. We built a computational model based on a variant of Discrete Element Method (DEM) that can capture arbitrarily shaped particles via their level sets—called Level Set Discrete Element Method (LS-DEM). The full description of LS-DEM can be found here (Kawamoto et al., 2016). For our simulations, we directly imported the initial configuration for one of the packings as shown in Fig. B.1 and applied a uniaxial displacement to the packing constrained by the box to determine its constrained modulus. Frictional forces between the particles and observation window have been neglected in the DEM simulations to model the experiments. The results are in good agreement with the values obtained from the experimental data. The simulations were ran with coefficient of friction $\mu = 0.6$, density $\rho = 1250$ kg m^{-3}, normal stiffness $k_n = 20{,}000$ N/m, shear stiffness $k_s = 9000$ N/m and total strain of 10 percent in the vertical directions while applying a no displacement boundary condition laterally. The application of the vertical strain is done in 5000 time steps to ensure a quasi-static loading. The obtained constrained modulus is $E = 4.062$ MPa which is in good agreement with those obtained from our hybrid experimental–mechanical setup (see Fig. B.2).

Appendix C. Supplementary data

Supplementary material related to this article can be found online at https://doi.org/10.1016/j.jmps.2022.104912.

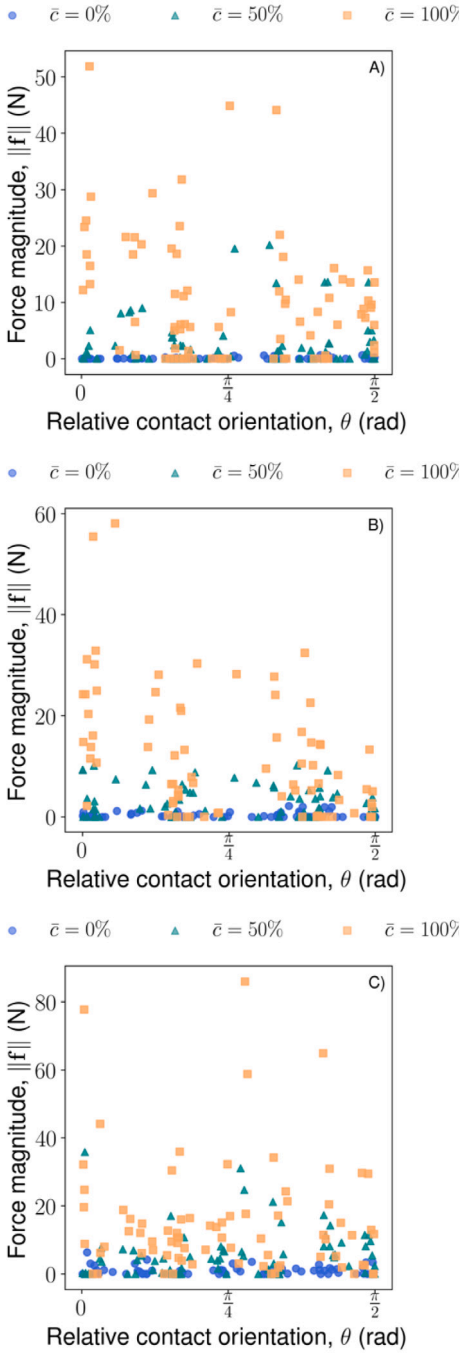

Fig. A.2. Evolution of fluid pressure, effective stress, and their summation as a function of time for three different configurations of granular matter. Each symbol represents data gathered at a certain consolidation (time). Experimental results with the shaded region capturing the range of results for various configurations. The evolution of effective stress is calculated directly from the inter-particle forces obtained using GEM.

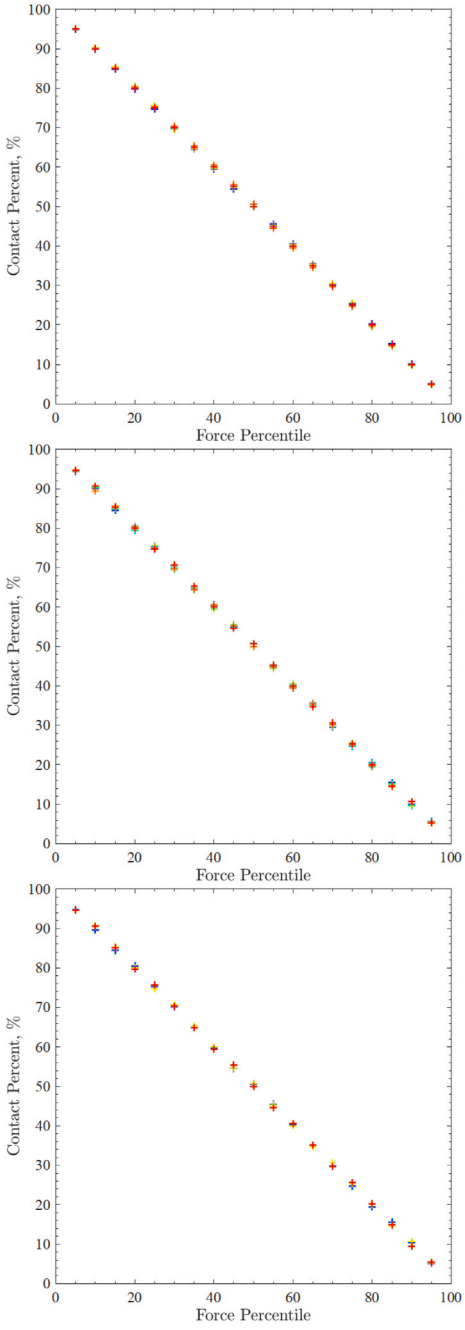

Fig. A.3. Scatter plots of force magnitude and contact orientation relative to the direction of load application for experiments 1 (A), 2 (B) and 3(C), showing clear increases in magnitude of force as consolidation evolves, especially in the direction of loading ($\theta = 0$).

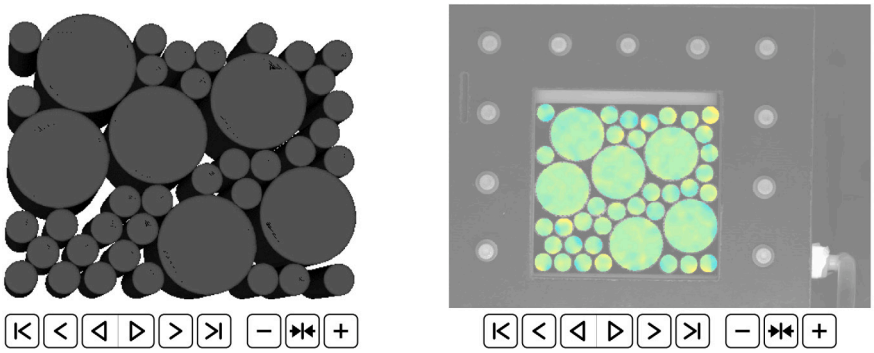

Fig. B.1. An example of LS-DEM simulations (left) with the imported initial configuration from the experiment (right).

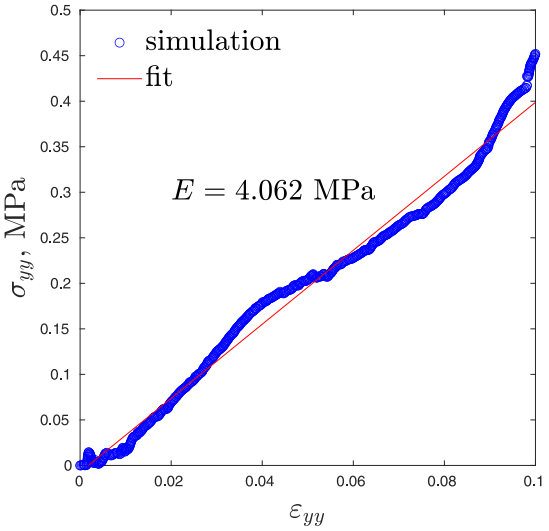

Fig. B.2. The axial stress σ_{yy} vs. the axial strain ε_{yy} curve for obtaining the constrained modulus ($E = 4.062$ MPa) for one of the configurations explored in experiments.

References

Andrade, J., Borja, R., 2007. Modeling deformation banding in dense and loose fluid-saturated sands. Finite Elem. Anal. Des. 43, 361–383.

Andrade, J., Lim, K., Avila, C., Vlahinic, I., 2012. Granular element method for computational particle mechanics. Comput. Methods Appl. Mech. Engrg. 241–244, 262–274.

Atkin, R., Craine, R., 1976. Continuum theories of mixture: basic theory and historical development. Q. J. Mech. Appl. Math. 29, 209–244.

Biot, M.A., 1941. General theory of three-dimensional consolidation. J. Appl. Phys. 12 (2), 155–164.

Borja, R., 2004. Cam-Clay plasticity. Part V: A mathematical framework for three-phase deformation and strain localization analyses of partially saturated porous media. Comput. Methods Appl. Mech. Eng. 193, 5301–5338.

Cappa, F., Scuderi, M.M., Collettini, C., Guglielmi, Y., Avouac, J.-P., 2019. Stabilization of fault slip by fluid injection in the laboratory and in situ. Sci. Adv. 5 (3), eaau4065.

Christensen, J., 2010. Modeling diffusion-induced stress in Li-ion cells with porous electrodes. J. Electrochem. Soc. 157 (3), A366.

Christoffersen, J., Mehrabadi, M.M., Nemat-Nasser, S., 1981. A micromechanical description of granular material behavior. J. Appl. Mech. 48, 339–344.

Coussy, O., 2004. Poromechanics. John Wiley & Sons.

Daniels, K.E., Kollmer, J.E., Puckett, J.G., 2017. Photoelastic force measurements in granular materials. Rev. Sci. Instrum. 88 (5), 051808.

Donald, K.M., Ravichandran, G., 2019. Confocal microscopy and digital volume correlation methods for intergranular force transmission experiments. Exp. Tech. 43, 457–468.

Faunt, C.C., Sneed, M., Traum, J., Brandt, J.T., 2016. Water availability and land subsidence in the central valley, California, USA. Hydrogeol. J. 24 (3), 675–684.

Galindo-Torres, S.A., Zhang, X., Krabbenhoft, K., 2018. Micromechanics of liquefancion in granular materials. Phys. Rev. A 10, 064017.

Holtz, R.D., Kovacs, W.D., Sheahan, T.C., 1981. An Introduction to Geotechnical Engineering, Vol. 733. Prentice-Hall Englewood Cliffs, NJ.

Hurley, R., Hall, S., Andrade, J., Wright, J., 2016. Quantifying interparticle forces and heterogeneity in 3D granular materials. Phys. Rev. Lett. 117, 098005.

Hurley, R., Marteau, E., Ravichandran, G., Andrade, J.E., 2014. Extracting inter-particle forces in opaque granular materials: beyond photoelasticity. J. Mech. Phys. Solids 63, 154–166.

Jiang, J., Lapusta, N., 2016. Deeper penetration of large earthquakes on seismically quiescent faults. Science 352 (6291), 1293–1297.

Kawamoto, R., Andò, E., Viggiani, G., Andrade, J.E., 2016. Level set discrete element method for three-dimensional computations with triaxial case study. J. Mech. Phys. Solids 91, 1–13.

Kuhn, M.R., Daouadji, A., 2020. Simulation of undrained quasi-saturated soil with pore pressure measurements using a discrete element (DEM) algorith. Soils Found. 60, 1097–1111.
Ladd, C.R., Reber, J.E., 2020. The effect of a liquid phase on force distribution during deformaiton in a granular system. JGR Solid Earth 125, e2020JB019771.
Lu, N., 2020. Unsaturated soil mechanics: Fundamental challenges, breakthroughs, and opportunities. J. Geotech. Geoenviron. Eng. 146 (5), 02520001.
Mahabadi, N., Jang, J., 2017. The impact of fluid flow on force chains in granular media. Appl. Phys. Lett. 110, 041907.
Majmudar, T.S., Behringer, R.P., 2005. Contact force measurements and stress-induced anisotropy in granular materials. Nature 435 (7045), 1079–1082.
Monfared, S., Laubie, H., Radjai, F., Pellenq, R., Ulm, F.-J., 2017. Mesoscale poroelasticity of heterogeneous media. J. Nanomech. Micromech. 7 (4), 04017016.
Monfared, S., Zhou, T., Andrade, J.E., Ioannidou, K., Radjaï, F., Ulm, F.-J., Pellenq, R.J.-M., 2020. Effect of confinement on capillary phase transition in granular aggregates. Phys. Rev. Lett. 125 (25), 255501.
Notbohm, J., Kim, J.-H., Asthagiri, A., Ravichandran, G., 2012. Three-dimensional analysis of the effect of epidermal growth factor on cell-cell adhesion in epithelial cell clusters. Biophys. J. 102 (6), 1323–1330.
Odell, G., Oster, G., Burnside, B., Alberch, P., 1980. A mechanical model for epithelial morphogenesis. J. Math. Biol. 9 (3), 291–295.
Ovando-Shelley, E., Tamez Gonzalex, E., Santoyo Villa, E., 1997. Options for correcting differential settlements in Mexico city's Metropolitan Cathedral. In: 14th International Conference on Soil Mechanics and Foundation Engineering. Hamburg.
Prevost, J., 1980. Mechanics of continuous porous media. Internat. J. Engrg. Sci. 18, 787–800.
Rice, J.R., Rudnicki, J.W., Platt, J.D., 2014. Stability and localization of rapid shear in fluid-saturated fault gouge: 1. Linearized stability analysis. J. Geophys. Res. Solid Earth 119 (5), 4311–4333.
Rothenburg, L., Salvadurai, A., 1981. A micromechanical definition of the Cauchy stres tensor for particulate media. In: Salvadurai, A. (Ed.), Mechanics of Structured Media. pp. 469–486.
Simo, J.C., Hughes, T.J., 2006. Computational Inelasticity, Vol. 7. Springer Science & Business Media.
Smith, M.B., Montgomery, C., 2015. Hydraulic Fracturing. Crc Press.
Sunyer, R., Conte, V., Escribano, J., Elosegui-Artola, A., Labernadie, A., Valon, L., Navajas, D., García-Aznar, J.M., Muñoz, J.J., Roca-Cusachs, P., et al., 2016. Collective cell durotaxis emerges from long-range intercellular force transmission. Science 353 (6304), 1157–1161.
Sutton, M.A., Orteu, J.J., Schreier, H., 2009. Image Correlation for Shape, Motion and Deformation Measurements: Basic Concepts, Theory and Applications. Springer Science & Business Media.
Terzaghi, K., 1925. Erdbaumechanik Auf Bodenphysikalischer Grundlage. Leipzig u. Wien, F. Deuticke.
Zohdi, T., Wriggers, P., 2005. An Introduction to Computational Micromechanics. Springer.